RESEARCH ARTICLE

Check for updates

Distinguishing and unraveling classical and non-classical pathways in MFI zeolite crystallization: insights into their contributions and impact on the final product†

Jiayu Yu,[a] Ke Du,[a] Di Pan,[a] He Li,[b] Ling Ding,[a] Wei Chen,[a] Yahong Zhang [ID] *[a] and Yi Tang [ID] [a]

Simplifying complex synthesis systems containing multiple species into ones with a single classical or non-classical growth path is valuable for understanding their respective mechanisms. However, most zeolite growth involves intertwined classical and non-classical mechanisms, making it crucial to distinguish and modulate their contributions in the original synthetic system. In this study, we presented a method to distinguish and directly quantify the contributions of classical and non-classical crystallization pathways in MFI zeolite synthesis, demonstrating that the dominant pathway could be shifted from non-classical to classical by varying the H_2O/SiO_2 and ethanol/SiO_2 ratios. Our findings showed that reducing the H_2O/SiO_2 ratio favored the non-classical pathway, while increasing the ethanol/SiO_2 ratio promoted the classical mechanism. However, these changes had minimal effect on their crystallization sequences: the non-classical pathway predominated initially, but both pathways intertwined as crystallization progressed. Notably, the shift in crystallization pathway did not significantly affect the acidic properties of the zeolites but had a direct impact on their catalytic performance. The catalytic activity of the resulting ZSM-5 zeolites in furfuryl alcohol etherification correlated with the contribution of the classical pathway, with higher contributions leading to enhanced catalytic activity. This study provides new insights into the zeolite crystallization process, offering a valuable approach for optimizing synthesis conditions and improving catalyst performance.

1. Introduction

Zeolites, as important open-framework materials, are extensively utilized in fields ranging from energy catalysis to environmental protection,[1–4] owing to their exceptional thermal and hydrothermal stability, diverse porosity, and tunable acidity. Studies show that these properties, crucial for their applications, are significantly influenced by the size, morphology and structural properties of the crystals.[5–7] However, developing materials with predictable physicochemical properties remains a challenge *via* a simply regulated

crystallization process, primarily due to the complex and often poorly understood mechanisms of zeolite crystallization. Factors such as synthetic sources, chemical composition, crystallization conditions, and synthesis methods all contribute to this complexity. Moreover, the diversity of zeolite growth units and the variable sequence of events governing zeolite formation further complicate the crystallization process.[8–11]

It is now understood that zeolite crystallization process involves both classical and non-classical pathways driven by diverse growth units ranging from molecules to nanoparticles.[12–14] The classical pathway, characterized by the layer-by-layer addition of soluble silica molecules (*i.e.*, ions or molecules) to specific crystal surface sites (*i.e.*, kinks, steps, edges, and terraces), has been the cornerstone of crystallization theory for centuries. However, emerging research into non-classical crystallization, which occurs through particle attachment, has led to new insights into zeolite formation. This mechanism, which operates alongside classical crystallization, is particularly important for understanding the controlled synthesis of zeolites with desired properties.[15–17] Despite these advances, distinguishing between these path-

[a]*Department of Chemistry, Shanghai Key Laboratory of Molecular Catalysis and Innovative Materials, State Key Laboratory of Porous Material for Separation and Conversion, Collaborative Innovation Centre of Chemistry for Energy Materials (iChEM), Fudan University, Shanghai 200433, P. R. China.*
E-mail: zhangyh@fudan.edu.cn
[b]*SINOPEC (Dalian) Research Institute of Petroleum and Petrochemicals Co., Ltd, Dalian 116045, Liaoning, China*

4048 | *Inorg. Chem. Front.*, 2025, **12**, 4048–4058

This journal is © the Partner Organisations 2025

ways and understanding their reciprocal effects remain key challenges. More recently, Yu and co-workers have revealed the critical role of silanol in the kinetic regulation of the zeolite non-classical crystallization process, demonstrating that particle addition preferentially occurs at high-density silanol surfaces, leading to the formation of high-aspect-ratio nanosheets due to anisotropic growth rates.[18] In our previous work, we achieved sole non-classical crystallization of zeolite in weakly alkaline and acidic environments and dual-pathway crystallization in a strongly alkaline condition using highly ordered zeolite subcrystals.[19] This led to a gradual evolution of the crystal morphologies from nanosheets to nanoparticles with increasing pH, which indicates intertwined interaction between the dual growth pathways, leading to a crystallization process that is different from those observed in single-pathway systems. Apparently, molecular addition influences oriented aggregation, thus yielding nanoparticles instead of nanosheets.[20] Nevertheless, most studies that investigate the role of classical or non-classical crystallization have focused on simplified systems, where soluble species or particles are separated. This limits the understanding of these mechanisms under real synthesis conditions, where soluble species and particles coexist.[21–23]

Moreover, the sol–gel system in zeolite synthesis is inherently complex, as characterized by the non-ergodic nature of the zeolite precursors,[16,24] including variations in the concentration and speciation of the (alumino)silicates, as well as the dynamic distribution between the amorphous solid and solution with time. These factors are significant obstacles in achieving a systematic understanding of the zeolite crystallization mechanisms. However, up to now, it has been shown that a number of zeolites can be produced from optically clear, homogenous solutions.[25–30] These transparent systems are ideally suited for complete characterization of zeolite precursors to gain insights into the evolution of (alumino)silicate species.[31] Among these, the synthesis of pure silica MFI (TPA-silicalite-1) serves as a model system.[32] This is due to its simple composition and well-defined two-step crystallization process—nucleation and growth—which can be monitored by light-scattering techniques.[33,34]

In this study, based on the MFI clear solution system, we successfully modulate and quantify the contributions of classical and non-classical pathways in the zeolite crystallization process by simply varying the water-to-silica and ethanol-to-silica ratios. These adjustments mainly affect the amounts of nuclei or soluble silica species, which in turn influence zeolite growth. By evaluating the key parameters of the typical S-shaped crystallization curves, such as the nucleation time, growth rates, particle morphology, zeolite yield, associated with the resultant catalytic performance, we offer new insights into the distinct roles of classical and non-classical pathways and their sequences throughout the crystallization process. This approach enables the direct study of the classical and non-classical mechanisms in an intact synthetic system, without the need to separate them, thus providing valuable guidance for further optimization of zeolite catalysts.

2. Experimental section

2.1. Chemical and materials

All of the following reagents were directly used without further purification: tetraethyl orthosilicate (TEOS) (99%, Sinopharm Chemical Reagent Co., Ltd), tetrapropylammonium hydroxide (TPAOH) (25 wt%, Sinopharm Chemical Reagent Co., Ltd), aluminum isopropoxide ($C_9H_{21}AlO_3$, 99.9%, Aladdin), deionized water (H_2O, Watsons), deuterium oxide (D_2O, 99.9 atom.% D, Aladdin), tetramethylsilane (TMS) ($C_4H_{12}Si$ ≥99.9%, Macklin), chloroform-d ($CDCl_3$, 99.8 atom.% D, Macklin), ethanol (C_2H_6O, ≥99.7%, Sinopharm Chemical Reagent Co., Ltd), dialysis tube (Spectra/Por 3, Spectrum Laboratories), isopropanol (C_3H_8O, ≥99.7%, Sinopharm Chemical Reagent Co., Ltd), furfuryl alcohol ($C_5H_6O_2$, 98%, Aladdin), 1,3,5-trimethylbenzene (C_9H_{12}, 97%, Macklin), pyridine (Py) (C_5H_5N, 99%, Alfa-Aesar), and 2,6-ditert-butylpyridine (BDMEP) ($C_{13}H_{21}N$, >97.0%, Aladdin).

2.2. Synthesis of nanosized MFI under different H_2O/SiO_2 ratios and solid product collection under different times of hydrothermal treatment

Silicalite-1 nano-zeolite was prepared by using an Anton Paar Monowave 400 microwave synthesizer under different H_2O/SiO_2 molar ratios. The sol composition was X SiO$_2$: 0.39 TPAOH: 13.21 H_2O: 4X ethanol, where X = 1.0–1.9. A representative synthesis for X = 1.0 is as follows: 5.287 g of TPAOH solution was added to 3.472 g of TEOS, and the obtained mixture was rapidly stirred at room temperature for 24 h to ensure complete hydrolysis. Thereafter, it was transferred into a 30 mL explosion-proof glass tube for a two-step heating process. Firstly, the solution was heated at 90 °C for 90 min under microwave irradiation, where the beginning time was defined as −90 min. Secondly, the obtained clear liquid was immediately heated at 130 °C, with sampling at intervals up to 600 min. Particle size evolution was monitored using dynamic light scattering (DLS). Once the system reached the inflection point indicated by DLS measurement, the solid samples during the linear growth stage were separated and purified from the mixed sol by using a two-step dialysis procedure. In detail, the clear solution was transferred into a dialysis tube with a molecular weight cutoff of 3.5 kDa, and then the sealed dialysis tube was immersed in 6 mmol L^{-1} TPAOH aqueous solution for 24 h. Subsequently, the dialysis tube was transferred and immersed into deionized water for 48 h, with the deionized water replaced every 12 h. Consequently, the purified sol was freeze-dried in vacuum at −50 °C, and solid yields were calculated after removing the structure-directing agent through calcination at 550 °C. For the collection of samples after the linear growth stage, the solids were separated by high-speed centrifugation, freeze-drying and calcination. Moreover, ZSM-5 nano-zeolites under different H_2O/SiO_2 molar ratios were synthesized using a similar method, but with the sol composition adjusted to X SiO$_2$: 0.39 TPAOH: 0.0025X Al$_2$O$_3$: 13.21 H_2O: 4X ethanol, where X = 1.0–1.9.

This journal is © the Partner Organisations 2025

Inorg. Chem. Front., 2025, **12**, 4048–4058 | **4049**

During the hydrothermal treatment, the solid product collection and treatment followed the same procedure.

2.3. Synthesis of nanosized MFI under different ethanol/SiO$_2$ ratios and solid product collection under different hydrothermal treatment times

The silicalite-1 nano-zeolites were synthesized under different ethanol/SiO$_2$ molar ratios by an aqueous clear sol composition of 1 SiO$_2$: 0.39 TPAOH: 13.21 H$_2$O: X ethanol, where X = 0–10. For X = 6, 5.287 g of TPAOH solution and 1.533 g of ethanol (EtOH) were added to 3.472 g of TEOS. The obtained mixture was then rapidly stirred at room temperature for 24 h to ensure complete hydrolysis. For X = 0, ethanol was removed by rotary evaporation at 35 °C prior to hydrothermal treatment. The same two-step heating procedure was applied as described above. Solid product purification, freeze-drying, and yield calculations followed the same approach as for the varying H$_2$O/SiO$_2$ ratios. ZSM-5 nano-zeolites were also synthesized using a modified sol composition of 1 SiO$_2$: 0.39 TPAOH: 0.0025 Al$_2$O$_3$: 13.21 H$_2$O: X ethanol, where X = 0–10, with the same solid collection and treatment methods.

2.4. Characterization

The particle size was measured by dynamic light scattering on a Malvern Zetasizer Nano-ZS90 instrument. Field emission scanning electron microscopy (SEM) images were obtained with a Hitachi S-4800 system. Field emission transmission electron microscopy (TEM) images were recorded on a Tecnai G2 F20 S-Twin apparatus. Argon adsorption/desorption characterization was performed at 87 K after degassing at 573 K for 7 h under vacuum on a Quantachrome iQ-2 physical adsorption instrument. All ^{29}Si nuclear magnetic resonance (NMR) spectra were obtained on a Bruker AVANCE III HD 500 MHz spectrometer. An appropriate amount of the supernatant (0.6–0.8 mL) was transferred into a 5 mm NMR quartz tube with a modified background-free commercial probe, and a small amount of D$_2$O was added into the tube for a lock signal. A solution of tetramethylsilane (TMS) in CDCl$_3$ was used as an external reference. It was shown that the monomer resonance was at −71.9 ppm relative to TMS, which was then used as an internal reference. The relative amount of Q^n in the oligomer fraction was calculated by decomposing the ^{29}Si NMR spectra.

The acidic properties of the ZSM-5 samples were obtained by temperature-programmed desorption of ammonia (NH$_3$-TPD) performed on the Micromeritics 2920 chemisorption analyzer. The quantitative analysis of the B/L acid type was completed via the Bruker Invenio S instrument Fourier-transform infrared spectrometer to collect the pyridine infrared (Py-IR) spectra. A self-supported wafer of the sample was placed in the IR cell, and evacuated at 450 °C for 75 min with a vacuum system. Reference spectra at 300 °C were recorded. Prior to collecting the Py-IR spectra, the outgassed samples were placed in pyridine vapor at room temperature for 15 min. The Py-IR spectra were collected after outgassing pyridine at 300 °C in a vacuum environment for 30 min. The

acid density of zeolite is calculated using the following formula:[35]

$$\text{Acid site density } (\mu\text{mol g}^{-1}) = \left(\frac{\text{peak area (cm}^{-1})}{\varepsilon(\text{cm } \mu\text{mol}^{-1})}\right) \times \left(\frac{a_{cs}\,(\text{cm}^2)}{m\,(\text{g})}\right)$$

where the peak area is calculated by integrating the peak area of the IR absorption peak, and ε stands for the molar extinction coefficient. For a Brønsted acid, ε(1545 cm^{-1}) = 0.96 (cm μmol^{-1}) and for Lewis acid, ε(1455 cm^{-1}) = 1.52 (cm μmol^{-1}).[36] In addition, a_{cs} represents the cross-sectional area of the wafer, and m is the mass of the wafer.

The element content and ratios in the products were analysed by inductively coupled plasma-atomic emission spectrometry (ICP) on a PE-8000 spectrometer. X-ray photoelectron spectroscopy (XPS) experiments were conducted on a Thermo Fisher Scientific K-Alpha (Al-Kα) X-ray photoelectron spectrometer to analyze the surface Si/Al ratio of the zeolite. Powder X-ray diffraction (XRD) data of all materials were collected using the Bruker D2 powder diffractometer to determine the phase of product. The X-ray wavelength was 1.54056 Å, with operating voltage and current set at 30 kV and 10 mA, respectively. Attenuated total reflectance-Fourier transform infrared spectroscopy (ATR-FTIR) experiments were conducted by a Spectrum Two Spectrometer (PerkinElmer) using a diamond ATR detector.

2.5. Catalytic reactions

The etherification of furfuryl alcohol (FAL) and isopropanol was carried out in an Anton Paar Monowave 400 microwave synthesizer. In a 30 mL microwave reaction tube, 80 mg of catalyst was added, along with 6 g (100 mmol) of isopropanol, 0.49 g (5 mmol) of furfuryl alcohol, and 100 mg of 1,3,5-trimethylbenzene, which is the internal standard. After thorough stirring, the tube was placed into the microwave reactor and heated at 110 °C for 2 h. Then, the products were analyzed on a Shimadzu 2010 plus gas chromatography (GC) system to calculate the conversion and selectivity of the catalytic reaction. The GC was equipped with an HP-5 chromatographic column (30 m × 0.32 mm × 0.25 μm) and a flame ionization detector (FID). As the etherification product of FAL, furfuryl isopropyl ether (FPE) was detect as the main product. The FAL conversion and product selectivity were calculated as follows: FAL conversion = moles of FAL reacted/moles of initial FAL × 100%, product selectivity = moles of FPE produced/moles of FAL reacted × 100%. Finally, the turnover numbers (TON) were calculated using the following equation:

$$\text{TON} = \frac{\text{number of FAL converted } (mol)}{\text{number of active sites } (mol)}$$
$$= \frac{\text{number of FAL converted } (mol)}{m\,(\text{g}) \div (60 \times \text{silicon to aluminium ratio})}$$

where m is the mass of the catalyst, and the silicon-to-aluminium ratio was determined by ICP-AES.

In addition, to exclude the influence of active sites distributed on the external surface, experiments using hindered pyri-

4050 | *Inorg. Chem. Front.*, 2025, **12**, 4048–4058

This journal is © the Partner Organisations 2025

dine (2,6-di*tert*-butylpyridine, BDMEP) were performed by the addition of excess amounts of BDMEP into the solution of isopropanol containing the catalyst, and stirring for 12 h. Subsequently, the poisoned catalyst was obtained by washing with isopropanol to remove unabsorbed BDMEP. Then, the catalytic tests were performed in the same way as the above mentioned process.

3. Results and discussion

3.1. Distinguishing and quantifying the crystallization pathway in the MFI synthetic system

3.1.1. Effect of the H_2O/SiO_2 ratio on the crystallization pathway. Zeolites are mostly synthesized under hydrothermal condition, where the H_2O content relative to the solute directly influences the solute supersaturation, ultimately determining the rates of zeolite nucleation and growth. Instead of diluting the synthesis mixtures with water, herein, we change the silica content while keeping the water content constant to investigate the effect of the H_2O/SiO_2 ratio, thereby minimizing the impact of changes in the alkalinity ($TPAOH/H_2O$). Silicalite-1 zeolites with varying H_2O/SiO_2 ratios were prepared using a molar composition X SiO_2: 0.39 TPAOH: 13.21 H_2O: $4X$ C_2H_5OH (X = 1.0, 1.3, 1.6, 1.9). During the hydrothermal treatment, dynamic light scattering (DLS) was used to monitor the particle size changes in the mother liquor. As expected, all the crystallization processes displayed a typical S-shaped curve (Fig. 1), which could be easily divided into nucleation and crystal growth stages, separated by an "inflection point" characterized by rapid size changes. A reduction in the $H_2O/$ SiO_2 ratio results in an extended nucleation period (from 45 min to 125 min, Table 1, entries 1 and 7), accompanied by a slowdown in the crystal growth rate (from 1.13 nm min^{-1} to 0.62 nm min^{-1}, Fig. 1). Given that in the synthesis system where the H_2O content is fixed, a decrease in the H_2O/SiO_2 ratio will lead to a relative increase in the ethanol content due to the hydrolysis of TEOS in the sol. This suggests that ethanol may slow down the crystallization dynamics, including both the nucleation period and the growth rate. As shown in Fig. S1,† removing ethanol from the initial sol with a H_2O/SiO_2 ratio of 10.16 results in a significant reduction in the nucleation period (from 65 min to 15 min) and an acceleration in the crystal growth rate (from 0.87 nm min^{-1} to 2.61 nm min^{-1}), which is even faster than the ethanol-containing system with a H_2O/SiO_2 ratio of 13.21. Therefore, the observed decrease in crystallization kinetics with a lower H_2O/SiO_2 ratio can be ascribed to the effect of ethanol. Possible reasons for this are discussed below (*vide infra*).

A two-step dialysis program was employed at the inflection point and in the early growth stage to remove soluble monomer silica species and excess TPA$^+$ ions.[20,37,38] The nanoparticles obtained by dialysis at the inflection point are nuclei with high short-range ordering, as revealed in our previous reports.[20] According to the previous studies,[20,37,38] these nanoparticles contributed to non-classical crystallization *via* aggregation. Therefore, the solid yield obtained at the inflection point represents the contribution of non-classical crystallization to the final product. Also, the total zeolite crystal yield is the sum of classical and non-classical crystallization pathways due to the well-established dual growth model for zeolite crystallization.[20] Thus, the difference between the yield of the
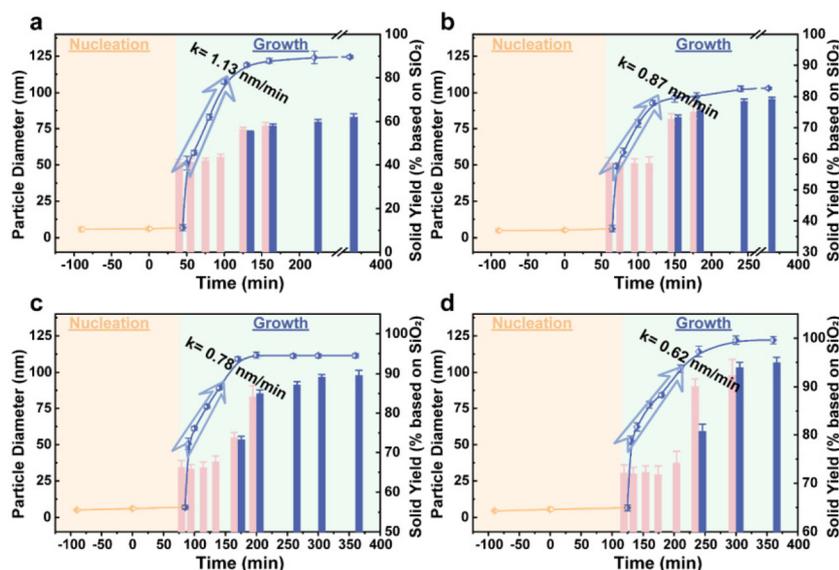
Fig. 1 Sizes and solid yields of silicalite-1 zeolite particles synthesized with different H_2O/SiO_2 molar ratios under different hydrothermal treatment times: (a) 13.21; (b) 10.16; (c) 8.26; (d) 6.95. The curves represent particle diameters, while the bar charts show the solid yields obtained by dialysis (pink) or centrifugation (blue) after removing the structure-directing agent *via* calcination at 550 °C. Error bars indicate the standard deviation (SD). The data for particle size are presented as the mean ± SD (n = 6), and those for yield are presented as the mean + SD (n = 4).

This journal is © the Partner Organisations 2025

Inorg. Chem. Front., 2025, **12**, 4048–4058 | **4051**

Table 1 Summary of the growth process and final products under different H_2O/SiO_2 ratios for the MFI zeolite

| Entry | Initial gel composition | | Nucleation period (min) | Contribution to total zeolite yield (wt%) | | Total yield of zeolite [c] | Size[d] (nm) |
	H_2O/SiO_2	Si/Al		Non-classical pathway[a]	Classical pathway[b]		
1[e]	13.21	∞	45	41.4%	20.8%	62.2%	125
2[e]		200	65	46.1%	18.5%	64.6%	164
3	10.16	∞	65	58.8%	20.5%	79.3%	103
4		200	70	59.8%	21.4%	81.2%	125
5	8.26	∞	85	67.7%	21.9%	89.6%	111
6		200	80	68.7%	21.3%	90.0%	120
7	6.95	∞	125	72.2%	22.8%	95.0%	122
8		200	110	77.3%	20.8%	98.1%	133

[a] Expressed by the yield of nuclei obtained *via* dialysis at the growth inflection point. [b] Expressed as the difference between the yield of the final zeolite and the yield of nuclei. [c] The corresponding yields of the final product obtained by centrifugation. [d] Measured by DLS, with the average of the 6 test results taken. [e] The sample also represents the one with an ethanol/SiO_2 ratio of 4. All yields were calculated after removing the structure-directing agent by calcination at 550 °C, with the average of the 4 results taken.

nuclei and final crystal yield reflects the contribution of the classical crystallization pathway. As shown in Table 1 (entries, 1, 3, 5 and 7), the contribution of the non-classical pathway increases significantly as the ratio of H_2O/SiO_2 ratio decreases, while the classical pathway remains essentially unchanged, totally leading to an increase in the zeolite product, indicating the very different effects of the H_2O/SiO_2 ratio on the two crystallization routes. However, a marked increase in the nucleation number at a lower H_2O/SiO_2 ratio does not lead to a significant decrease in the final nano-zeolite size (Table 1, entries 1, 3, 5 and 7). This observation contrasts with the conventional conclusion of the existing literature, where the small amounts of nuclei lead to larger crystals, while higher (alumino)-silicate concentrations are desirable for producing more nuclei and minimizing the ultimate crystal sizes.[39–41] This could be attributed to the high nucleation density in our synthetic systems, even with a minimum nucleation of up to 41.4%.

The bar charts In Fig. 1 show the solid yields over time during the hydrothermal treatment. These yields in the early growth stage, calculated by the solid obtained *via* dialysis, provide an accurate representation of zeolite crystallization, as dialysis selectively removes the soluble species while retaining all the solid species, including growing the zeolite crystals, untransformed nuclei particles and soluble monomers that have already been incorporated into particles during growth, as shown in Fig. S2.† [20,37,38] Interestingly, the solid yields during the linear growth stage remain relatively constant and nearly equal to the yield at the inflection point (Fig. 1), even as the growth rate slows to 0.62 nm min⁻¹. This suggests that non-classical crystallization predominates during the early linear growth stage. If the crystal growth process involves the addition of soluble species during this period, the solid yield will be higher than that of nuclei at the flection point and gradually increase over time. A sharp increase in the solid yields after the end of the linear growth period indicates the involvement of single-molecule addition *via* classical crystallization pathway in this period. Therefore, the sequence of events governing zeolite formation, which is not significantly

affected by the H_2O/SiO_2 ratio, is characterized by predominant non-classical growth during the early linear growth stage, followed by a shift to classical crystallization in the later stage. Further crystallization studies (Fig. S3†) show that during the linear growth period, the crystals formed at different H_2O/SiO_2 ratios exhibit a rough surface due to the dominant nuclei aggregation. As crystallization progresses, the surface morphologies of the crystals evolve from rough to relatively smooth, supporting the proposed mechanism of non-classical crystallization followed by classical growth.

Additionally, the introduction of the aluminum species into the silicalite-1 system with different H_2O/SiO_2 ratios leads to the formation of the ZSM-5 zeolite, with similar crystallization behavior to silicalite-1. As shown in Fig. S4,† the crystallization kinetics of the ZSM-5 zeolites follow the same trend as that for silicalite-1, where a lower H_2O/SiO_2 ratio results in a longer nucleation time, from 65 min to 110 min (Table 1, entries 2 and 8), and a reduction in the linear growth rate from 1.22 nm min⁻¹ to 0.59 nm min⁻¹. Dialysis yields remain unchanged during in the linear stage, but increase at the later stage, once again indicating that non-classical crystallization routes dominate early on, with classical crystallization becoming more prevalent later. Moreover, in terms of thermodynamics, the increase in the silica content, *i.e.*, a decrease in the H_2O/SiO_2 ratio, leads to an improvement in the zeolite yield, from 64.6% to nearly 100%, by increasing the contribution of non-classical crystallization. Meanwhile, the classical pathway remains relatively constant, contributing approximately 20%, which aligns with observations in silicalite-1 (Table 1). Inductively coupled plasma emission spectrometer (ICP) tests reveal a very low aluminum content in the supernatant with a Si/Al ratio exceeding 3000 (Table S1†), effectively indicating 100% utilization of the aluminum species. Consequently, as the H_2O/SiO_2 ratio decreases, the Si/Al ratio in the final product increases, owing to the increase of the zeolite yield (Table 3).

Although the introduction of aluminum did not affect the contribution of the H_2O/SiO_2 ratio to classical and non-classical crystallization as well as their sequence, it did influence

the nucleation time. Specifically, the nucleation time increases in systems with low silica–alumina concentrations (Table 1, entries 1 vs. 2 and 3 vs. 4), while they decrease in high silica–alumina systems (Table 1, entries 5 vs. 6 and 7 vs. 8). Furthermore, it is noteworthy that the introduction of just 0.5 mol% aluminum species displays a minimal effect on the non-classical growth, i.e., the linear growth rate does not change significantly, but the time required for the classical crystallization is markedly prolonged (about 1 h vs. 2.5 h) at essentially unchanged total molecular additions (around 20%), which means the rate of classical crystallization slows down significantly (Fig. 1 and Fig. S4†). In summary, aluminum additions have a kinetic impact, but have a slight influence on the impact of the H_2O/SiO_2 ratio on the crystallization pathway. Namely, similar to silicalite-1, reducing the H_2O/SiO_2 ratio is thermodynamically more favourable for non-classical crystallization, while it does not change the sequence of events governing zeolite formation.

3.1.2. Effect of the ethanol/SiO_2 ratio on the crystallization pathway.

Solvents play a crucial role in zeolite synthesis, influencing the solubility and reactivity of the (alumino)silicate species, thus controlling the zeolite nucleation and growth rates.[42–44] In the case of silicalite-1 synthesis, ethanol acts as both a co-solvent and an additive. As expected, variations of the ethanol content display a remarkable effect on the crystallization process of silicalite-1. It is clearly observed in Fig. 2 that increasing the ethanol/SiO_2 ratio extends the nucleation period by approximately nine-fold (from 15 min to 130 min), and decreases the crystal growth rate by about three-fold (from 2.18 nm min^{-1} to 0.60 nm min^{-1}). The addition of ethanol can modify the interaction strength among the silicate species, ethanol, water and organic cations.[43,45,46] To confirm this further, a single nuclei solution devoid of soluble silica species, obtained via a two-step dialysis procedure at the growth inflection point,[19] was employed to study their aggregation growth process. Similar to the above synthetic system, the addition of ethanol slowed the crystal growth rate (Fig. S5†). It is believed that ethanol can be adsorbed on the surface of the nuclei, inhabiting or slowing their growth.[47] It also confirms that, for the case of the H_2O/SiO_2 ratio effect, the slowdown in the nucleation period and crystal growth rate with decreasing H_2O/SiO_2 ratio is due to the increase of the ethanol content caused by the higher amount of TEOS at the lower H_2O/SiO_2 ratio, affecting the kinetics of crystallization.

Moreover, it is surprising that the addition of ethanol slightly reduces the contribution of the non-classical crystallization pathway, while greatly enhancing the classical crystalli-
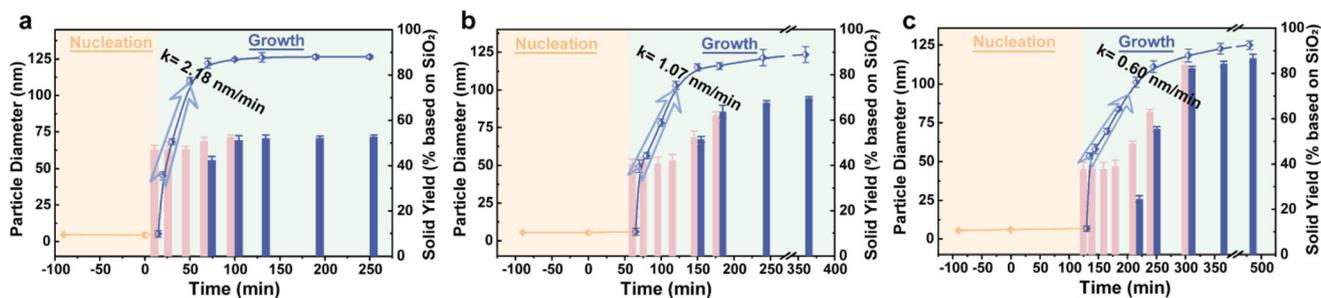
Fig. 2 Sizes and solid yields of silicalite-1 zeolite particles synthesized with different ethanol/SiO_2 molar ratios under different hydrothermal treatment times: (a) 0; (b) 6; (c) 10. The curves represent particle diameters, while the bar charts show the solid yields obtained by dialysis (pink) or centrifugation (blue) after removing the structure-directing agent via calcination at 550 °C. Error bars indicate the standard deviation (SD). The data for particle size are presented as the mean ± SD (n = 6) and those for yield are presented as the mean + SD (n = 4).

Table 2 Summary of the growth process and final products under different ethanol/SiO_2 ratios for the MFI zeolite

| Entry | Initial gel composition | | Nucleation period (min) | Contribution to total zeolite yield (wt%) | | Total yield of zeolite[c] | Size[d] (nm) |
	EtOH/SiO_2	Si/Al		Non-classical pathway[a]	Classical pathway[b]		
1	0	∞	15	46.9%	5.8%	52.7%	126
2		200	35	48.4%	9.2%	57.6%	135
3	6	∞	65	40.7%	28.9%	69.6%	123
4		200	80	44.6%	29.9%	74.5%	156
5	10	∞	130	37.7%	49.0%	86.7%	125
6		200	125	43.9%	48.2%	92.1%	142

[a] Expressed by the yield of nuclei obtained via dialysis at the growth inflection point. [b] Expressed as the difference between the yield of the final zeolite and the yield of nuclei. [c] The corresponding yields of the final product obtained by centrifugation. [d] Measured by DLS, with the average of the 6 test results taken. All yields were calculated after removing the structure-directing agent by calcination at 550 °C, with the average of the 4 results taken.

This journal is © the Partner Organisations 2025

Inorg. Chem. Front., 2025, **12**, 4048–4058 | **4053**

zation pathway (Table 2). For example, as the ethanol/silica ratio increases from 0 to 10, the contribution of classical crystallization to the final product increases markedly from 5.8% to 49.0% (Table 2, entries 1, 3 and 5). This means that ethanol promotes the addition of soluble silica molecules toward the crystal. However, the greater addition (around 40%) of the single molecule seems to have a minimal effect on the final particle size. The ethanol may interfere with the aggregation of nuclei, leading to the formation of more, but smaller, particles *via* the non-classical pathway in systems with higher ethanol content. Furthermore, similar to the observations with varying the H_2O/SiO_2 ratio, the solid yield during the linear growth stage remains relatively constant and increases significantly only in the later stages (Fig. 2). This indicates that the sequence of events governing zeolite formation remains unaffected by changes in the ethanol/SiO_2 ratio. Additionally, SEM images (Fig. S6†) show that the crystal morphologies also experience a change from rough surfaces during the linear growth period to relatively smooth ones at later stages, further supporting the sequential dominance of non-classical and classical growth mechanisms.

To further verify the role of ethanol in promoting the classical pathway (soluble silica species addition), ethanol (at an ethanol/Si ratio of 10) was added into a synthetic system initially lacking ethanol (ethanol/Si = 0) at the end of the linear growth stage (50 min). The addition results in an increase in both the size and yield of the final zeolite (Fig. 3a). Furthermore, the identification of different soluble silica species and evolution of the silicon connectivity (expresses as Q^n, where n represents the number of siloxane bonds of a silicon nucleus) of the oligomers in the supernatant before

and after ethanol addition were realized by ^{29}Si nuclear magnetic resonance (NMR) spectra. The assignments of Q^n are displayed in Fig. 3c, which are all consistent with the existing literature on silicate speciation (from −71 to −73 ppm for Q^0, from −79 to −83 ppm for $Q^{1/2\Delta}$, from −86 to −91 ppm for $Q^{2/3\Delta}$, −92 to −100 ppm for Q^3, and from −100 to −108 ppm for Q^4).[48–50] Notably, the relative amount of the Q^3 site in all oligomers significantly increases after ethanol addition at 50 min. In particular, the cubic octamers (D4R) and double five-ring (D5R) (around −99 ppm) fraction become significant (Fig. S7†), confirming the positive role of ethanol in enhancing the condensation degree of oligomers and driving the evolution of silica species toward D4R and D5R. Once heated (>50 min), the amounts of Si in D4R and D5R significantly decrease (Fig. S7d†); in parallel, the corresponding yields markedly increase, which indicates that the existence of D4R and D5R units can drive the addition of soluble oligomers to the crystal (Fig. 3a). Furthermore, in the ethanol-added system, the residual soluble silica species in the final reaction system are reduced significantly compared to the initial system (Fig. 3c and d), further suggesting a high utilization rate of the silica species. Conversely, when ethanol is removed from a system with an initial ethanol/Si ratio of 10 at the end of the linear growth stage (215 min, Fig. 3b), an opposite trend is observed. Significant depolymerization of the D4R and D5R units occurs (Fig. S8†), along with notable reductions in the particle size and yield compared to systems where ethanol is retained (Fig. 3b), suggesting the inhibition of the soluble silica species addition process during the later stages of crystallization. Moreover, the significant increase of the residual soluble silica species in the final reaction mixture further sup-
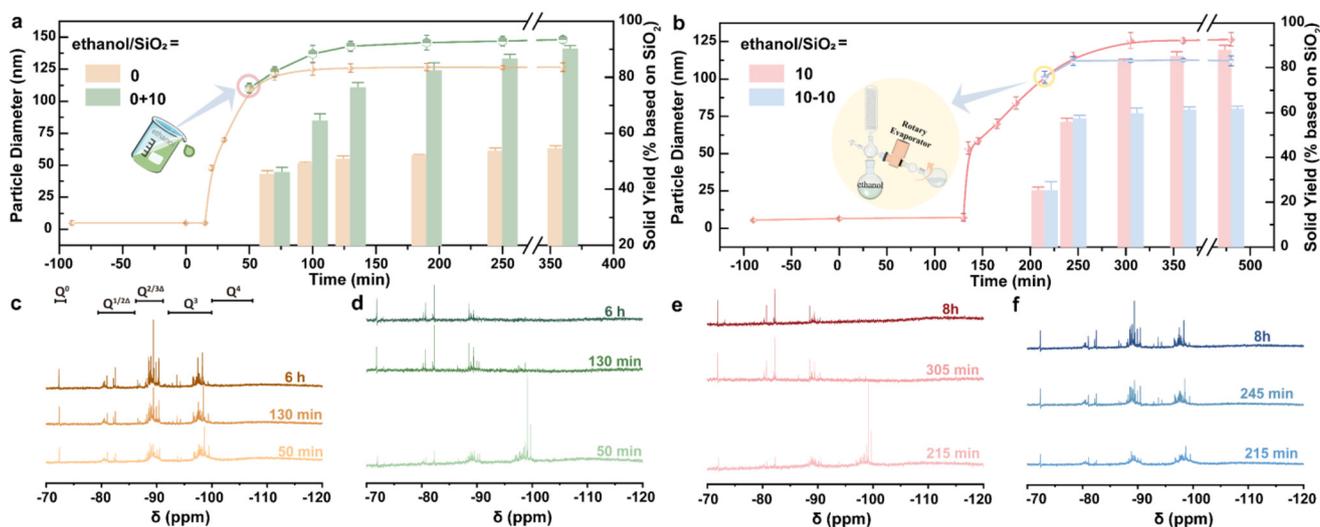
Fig. 3 Size and solid yields of silicalite-1 zeolite particles without or with ethanol addition (a), and without or with ethanol removal (b) during hydrothermal treatment. The curves represent particle diameters, while the bar charts show the solid yields obtained by centrifugation after removing the structure-directing agent *via* calcination at 550 °C. Error bars indicate the standard deviation (SD). The data for particle size are presented as the mean ± SD ($n = 6$), and those for yield are presented as the mean + SD ($n = 4$). ^{29}Si NMR spectra of the supernatants were obtained by centrifugation at different times before (c) and after (d) the addition of ethanol, and before (e) and after (f) the removal of ethanol. $Q^{n\Delta}$ indicates the Si site with n connectivity present in a 3-membered ring.

4054 | *Inorg. Chem. Front.*, 2025, **12**, 4048–4058

This journal is © the Partner Organisations 2025

ports the role of ethanol in facilitating the classical addition of monomers (Fig. 3e and f).

Finally, the introduction of aluminum into systems with varying ethanol/SiO_2 ratios reveals no significant changes in the relative contributions of classical and non-classical crystallization pathways, or the sequence of these processes (Fig. S9†). However, the incorporation of the aluminum species in systems with ethanol/SiO_2 ratios from 0 to 6 leads to a longer nucleation induction time, and a slower growth rate during the linear growth stage while they go in reverse in the system with an initial ethanol/Si ratio of 10. Ultimately, there is a higher zeolite yield at each alcohol-silica ratio system (Table 2, entries 1, 3, 5 *vs.* 2, 4 and 6). These findings indicate that ethanol offers a simple and effective approach to reversibly regulate the distribution of silicate species in oligomers while improving the final zeolite yield.

3.2. The impacts of different contributions of classical/non-classical pathway on the final product

Studies regarding the crystal engineering of zeolites have demonstrated that the regulation of the morphology and structure of zeolite can be achieved by altering the crystallization behaviours.[44,51–53] The above results show that the thermodynamic contributions of classical/non-classical crystallization are successfully quantified, showing a gradual shift from a non-classical route to the classical pathway by changing the H_2O/SiO_2 to ethanol/SiO_2 ratios. This transition is expected to impact the physicochemical properties of the resultant zeolites. Surprisingly, for the silicalite-1 nano-zeolites prepared under different H_2O/SiO_2 and ethanol/SiO_2 ratios, no significant difference in the morphological and structural features of the final products can be observed, as evidenced by the images of TEM and SEM, XRD patterns, and FTIR spectra, as well as Ar adsorption/desorption studies results (Fig. S10, S11 and Table S2†). Similarly, the ZSM-5 zeolite products with the addition of aluminum under these conditions also exhibit negligible differences in their morphological and structural features (Fig. S12, S13 and Table S3†).

Generally, the incorporation of an aluminum species can be used as an indicator of acidic and catalytic properties. NH_3 temperature-programmed desorption (NH_3-TPD) measurements show two well-defined desorption peaks for all ZSM-5 samples at around 145 °C and 340 °C, corresponding to the weak and strong acid sites (Fig. S14†), respectively. The quantitative analytic results in Table 3 show that the total acidity of all the samples correlate well with the Si/Al ratios, regardless of the synthesis conditions (different ethanol/SiO_2 ratios or H_2O/SiO_2 ratios). Meanwhile, pyridine infrared (Py-IR) spectra (Fig. S15†) further reveal comparable ratios of Brønsted acids (BAS) and Lewis (LAS) acids among all samples (Table 3). These results indicate that the changes in the crystallization pathway have minimal impact on the apparent acidic properties of the final zeolite crystals.

To further study the impact of the crystallization pathway on the product properties, furfuryl alcohol etherification was employed to evaluate their catalytic performances. Interestingly, the catalytic activities varied significantly with the proportion of the classical pathway contribution. As shown in Fig. 4a, the conversion of furfuryl alcohol (FAL) over various ZSM-5 zeolites follows the order of ZSM-5 prepared under ethanol/SiO_2 = 10 and H_2O/SiO_2 = 13.21 (ZSM-5-13.21-10) > the one with ethanol/SiO_2 = 4 and H_2O/SiO_2 = 13.21 (ZSM-5-13.21-4) > the one with H_2O/SiO_2 = 8.26 and ethanol/SiO_2 = 4 (ZSM-5-8.26-4). The contribution proportion of the classical pathway in the above three zeolite catalysts are 52.3%, 28.6% and 23.6%, respectively, correlating directly with their catalytic activities. This suggest that the ZSM-5 zeolite with a higher classical route contribution is prone to exhibit a higher catalytic activity. It is speculated that the differences in the classical and non-classical crystallization pathways influence the spatial distribution and micro-environment of aluminum at a mesoscopic level, thereby affecting their catalytic performance.

Moreover, due to their different bulk Si/Al ratios (and thus total acidic amounts), the turnover number (TON) values of the three catalysts were calculated to further elucidate their catalytic performances. Notably, ZSM-5-13.21-10 yields a TON of 480 for furfuryl alcohol etherification, nearly 50% higher than that of ZSM-5-13.21-4. For ZSM-5-13.21-4 and ZSM-5-8.26-4, an inverse trend is observed in the TON values compared to the conversion

Table 3 Acid properties of ZSM-5 samples prepared under different ethanol/SiO_2 ratios

| Entry | Initial gel composition | | NH$_3$-TPD | | | Py-IR | | | | |
| | H_2O/SiO_2 | EtOH/SiO_2 | Acid amount[a] ($\mu mol\ g^{-1}$) | | | Acid amount[b] ($\mu mol\ g^{-1}$) | | | | |
			Total	Weak acid	Strong acid	BAS	LAS	B/L	Si/Al (ICP-AES)	Si/Al (XPS)
1	13.21	4	174	97	77	82	23	3.6	89	78
2	10.16	4	155	86	69	73	18	4.1	104	73
3	8.26	4	145	80	65	57	15	3.8	120	67
4	6.95	4	118	70	48	51	14	3.6	132	64
5	13.21	0	193	108	85	102	25	4.1	79	73
6	13.21	6	156	91	65	75	18	4.2	98	78
7	13.21	10	124	69	55	66	17	3.9	123	83

[a] The weak and strong acid amounts were determined by the amounts of NH_3 desorbed at 100–250 °C and 250–450 °C, respectively. [b] The Brønsted and Lewis acid amounts were determined by Py-IR at 300 °C.
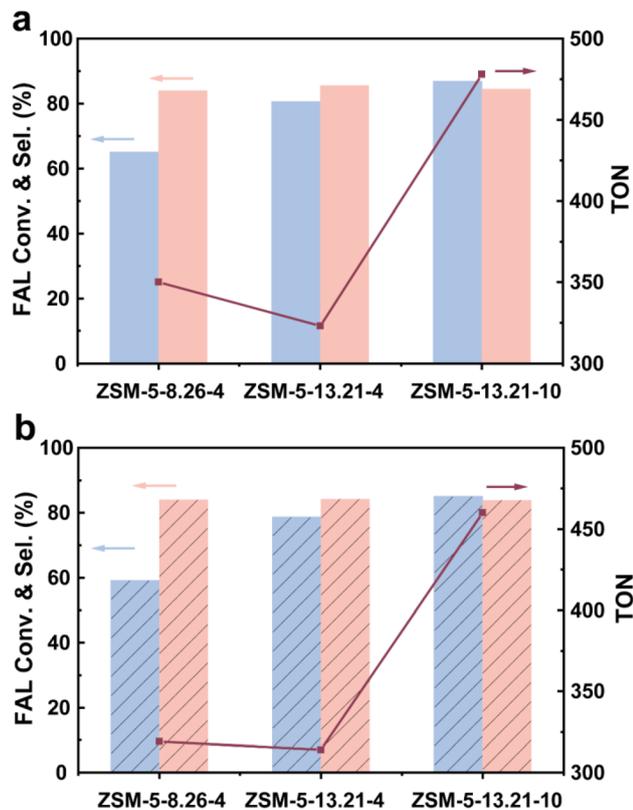
Fig. 4 Furfuryl alcohol etherification reaction catalyzed by fresh ZSM-5 zeolites with different H_2O/SiO_2 or ethanol/SiO_2 ratios (a), and by surface-passivated zeolites with 2,6-di-*tert*-butylpyridine (b).

of furfuryl alcohol. The TON value of ZSM-5-8.26-4 having a lower classical pathway contribution (23.6%) is slightly higher (8%) than that of ZSM-5-13.21-4 (Fig. 4a). It is worth mentioning that the furfuryl alcohol etherification reaction is prone to form carbon deposits, thus causing catalyst deactivation. Thus, a shorter diffusion pathway can improve the catalytic activity. Therefore, considering the smaller size (120 nm) and lower surface Si/Al ratio (67) of ZSM-5-8.26-4 than those of ZSM-5-13.21-4 (164 nm, surface Si/Al = 83), surface acid site passivation experiments using BDMEP adsorption were additionally adopted to exclude the influence of active sites distributed on the external surface (Fig. 4b). Even after passivation, the catalytic trends remained consistent. However, the TON values of ZSM-5-13.21-4 and ZSM-5-8.26-4 become comparable due to their similar classical pathway contributions. Therefore, the slight TON increase for ZSM-5-8.26-4 can be attributed to its smaller size and lower surface Si/Al ratio, whereas the significantly higher TON value for ZSM-5-13.21-10 is clearly linked to its higher classical pathway contribution in it.

4. Conclusion

In summary, we have successfully quantified the contributions of non-classical and classical crystallization pathways to the

final zeolite by calculating the yields of crystal nuclei and final zeolite. By varying the H_2O/SiO_2 to ethanol/SiO_2 ratios, we demonstrated that the dominant crystallization pathway of the MFI zeolite can shift from a non-classical route to a classical pathway. Specifically, reducing the H_2O/SiO_2 ratio promotes the formation of nuclei, favoring the non-classical route *via* particle attachment, while increasing the ethanol/silica ratio shifts the crystallization toward the classical route, enhancing the addition of soluble silicate molecules to the growing zeolite. The crystallization process revealed that, during the linear crystal growth stage, the non-classical pathway is dominant. However, as crystallization progresses, both classical and non-classical mechanisms begin to intertwine. Notably, such crystallization sequence is not affected by changes in the H_2O/SiO_2 and ethanol/SiO_2 ratios. More importantly, although the shifts in the crystallization pathway with varying H_2O/SiO_2 and ethanol/SiO_2 ratios have minimal impact on the apparent acidic properties of the final zeolite crystals, the catalytic performance of the resulting ZSM-5 zeolites in furfuryl alcohol etherification has been found to correlate directly with the proportion of the classical pathway. Zeolites with a higher classical pathway contribution exhibit significantly better catalytic activity, as evidenced by the higher conversion of furfuryl alcohol and TON. This study provides not only a method to directly distinguish, quantify and adjust the contribution of classical and non-classical crystallization, but also reveals their role in the catalytic performance, which is of great importance for advancing tailored zeolite synthesis.

Author contributions

The manuscript was written with contributions from all authors. All authors contributed extensively to the work presented in this paper. Jiayu Yu carried out the methodology, investigation, data curation, formal analysis, and writing of the original draft. Ke Du participated in data curation and analysis. Di Pan performed the methodology and investigation. He Li, Ling Ding and Wei Chen participated in the investigation. Yahong Zhang designed and directed the research, as well as contributed to the preparation and writing of the manuscript. Yi Tang participated in the analysis and discussion of the experimental results.

Data availability

The data supporting this article have been included as part of the ESI.†

Conflicts of interest

There are no conflicts to declare.

4056 | *Inorg. Chem. Front.*, 2025, **12**, 4048–4058

This journal is © the Partner Organisations 2025

Acknowledgements

References

1 M. E. Davis, Ordered porous materials for emerging applications, *Nature*, 2002, **417**, 813–821.

2 C. Martínez and A. Corma, Inorganic molecular sieves: Preparation, modification and industrial application in catalytic processes, *Coord. Chem. Rev.*, 2011, **255**, 1558–1580.

3 V. Valtchev, G. Majano, S. Mintova and J. Pérez-Ramírez, Tailored crystalline microporous materials by post-synthesis modification, *Chem. Soc. Rev.*, 2013, **42**, 263–290.

4 Y. Wei, T. E. Parmentier, K. P. de Jong and J. Zečević, Tailoring and visualizing the pore architecture of hierarchical zeolites, *Chem. Soc. Rev.*, 2015, **44**, 7234–7261.

5 Z. Lai, G. Bonilla, I. Diaz, J. G. Nery, K. Sujaoti, M. A. Amat, E. Kokkoli, O. Terasaki, R. W. Thompson, M. Tsapatsis and D. G. Vlachos, Microstructural optimization of a zeolite membrane for organic vapor separation, *Science*, 2003, **300**, 456–460.

6 Y.-J. Lee, J. S. Lee and K. B. Yoon, Synthesis of long zeolite-L crystals with flat facets, *Microporous Mesoporous Mater.*, 2005, **80**, 237–246.

7 F. Shi, X. Chen, L. Wang, J. Niu, J. Yu, Z. Wang and X. Zhang, Roselike microstructures formed by direct in situ hydrothermal synthesis: From superhydrophilicity to superhydrophobicity, *Chem. Mater.*, 2005, **17**, 6177–6180.

8 C. S. Cundy and P. A. Cox, The hydrothermal synthesis of zeolites: Precursors, intermediates and reaction mechanism, *Microporous Mesoporous Mater.*, 2005, **82**, 1–78.

9 K. Ding, A. Corma, J. A. Maciá-Agulló, J. G. Hu, S. Krämer, P. C. Stair and G. D. Stucky, Constructing Hierarchical Porous Zeolites via Kinetic Regulation, *J. Am. Chem. Soc.*, 2015, **137**, 11238–11241.

10 J. Grand, H. Awala and S. Mintova, Mechanism of zeolites crystal growth: new findings and open questions, *CrystEngComm*, 2016, **18**, 650–664.

11 J. D. Rimer, M. Kumar, R. Li, A. I. Lupulescu and M. D. Oleksiak, Tailoring the physicochemical properties of zeolite catalysts, *Catal. Sci. Technol.*, 2014, **4**, 3762–3771.

12 J. J. De Yoreo, P. U. P. A. Gilbert, N. A. J. M. Sommerdijk, R. L. Penn, S. Whitelam, D. Joester, H. Zhang, J. D. Rimer, A. Navrotsky, J. F. Banfield, A. F. Wallace, F. M. Michel, F. C. Meldrum, H. Cölfen and P. M. Dove, Crystallization by particle attachment in synthetic, biogenic, and geologic environments, *Science*, 2015, **349**, aaa6760.

13 A. I. Lupulescu and J. D. Rimer, In situ imaging of silicalite-1 surface growth reveals the mechanism of crystallization, *Science*, 2014, **344**, 729–732.

14 H. Zhang, H. Zhang, Y. Zhao, Z. Shi, Y. Zhang and Y. Tang, Seeding bundlelike MFI zeolite mesocrystals: A dynamic, nonclassical crystallization via epitaxially anisotropic growth, *Chem. Mater.*, 2017, **29**, 9247–9255.

15 M. Kumar, H. Luo, Y. Román-Leshkov and J. D. Rimer, SSZ-13 crystallization by particle attachment and deterministic pathways to crystal size control, *J. Am. Chem. Soc.*, 2015, **137**, 13007–13017.

16 R. Li, A. Chawla, N. Linares, J. G. Sutjianto, K. W. Chapman, J. G. Martínez and J. D. Rimer, Diverse physical states of amorphous precursors in zeolite synthesis, *Ind. Eng. Chem. Res.*, 2018, **57**, 8460–8471.

17 Y. Zhao, Z. Ye, L. Wang, H. Zhang, F. Xue, S. Xie, X.-M. Cao, Y. Zhang and Y. Tang, Engineering fractal MTW zeolite mesocrystal: Particle-Based dendritic growth via twinning-plane induced crystallization, *Cryst. Growth Des.*, 2018, **18**, 1101–1108.

18 Q. Zhang, J. Li, X. Wang, G. He, L. Li, J. Xu, D. Mei, O. Terasaki and J. Yu, Silanol-engineered nonclassical growth of zeolite nanosheets from oriented attachment of amorphous protozeolite nanoparticles, *J. Am. Chem. Soc.*, 2023, **145**, 21231–21241.

19 H. Li, J. Yu, K. Du, W. Li, L. Ding, W. Chen, S. Xie, Y. Zhang and Y. Tang, Synthesis of ZSM-5 zeolite nanosheets with tunable silanol nest contents across an ultra-wide pH range and their catalytic validation, *Angew. Chem., Int. Ed.*, 2024, **63**, e202405092.

20 Z. Sheng, H. Li, K. Du, L. Gao, J. Ju, Y. Zhang and Y. Tang, Observing a zeolite nucleus (subcrystal) with a uniform framework structure and Its oriented attachment without single-molecule addition, *Angew. Chem., Int. Ed.*, 2021, **60**, 13444–13451.

21 P. Sharma, J.-g. Yeo, M. H. Han and C. H. Cho, Knobby surfaced, mesoporous, single-phase GIS-NaP1 zeolite microsphere synthesis and characterization for H_2 gas adsorption, *J. Mater. Chem. A*, 2013, **1**, 2602–2612.

22 S. Teketel, L. F. Lundegaard, W. Skistad, S. M. Chavan, U. Olsbye, K. P. Lillerud, P. Beato and S. Svelle, Morphology-induced shape selectivity in zeolite catalysis, *J. Catal.*, 2015, **327**, 22–32.

23 Y. Zhao, H. Zhang, P. Wang, F. Xue, Z. Ye, Y. Zhang and Y. Tang, Tailoring the morphology of MTW zeolite mesocrystals: Intertwined classical/nonclassical crystallization, *Chem. Mater.*, 2017, **29**, 3387–3396.

24 L. L. Hench and J. K. West, The sol-gel process, *Chem. Rev.*, 1990, **90**, 33–72.

25 H. Awala, J.-P. Gilson, R. Retoux, P. Boullay, J.-M. Goupil, V. Valtchev and S. Mintova, Template-free nanosized faujasite-type zeolites, *Nat. Mater.*, 2015, **14**, 447–451.

26 S. Mintova, N. H. Olson, J. Senker and T. Bein, Mechanism of the transformation of silica precursor solutions into si-MFI zeolite, *Angew. Chem., Int. Ed.*, 2002, **41**, 2558–2561.

27 S. Mintova, N. H. Olson, V. Valtchev and T. Bein, Mechanism of zeolite A nanocrystal growth from colloids at room temperature, *Science*, 1999, **283**, 958–960.

This journal is © the Partner Organisations 2025

Inorg. Chem. Front., 2025, **12**, 4048–4058 | **4057**

28 S. Mintova, N. Petkov, K. Karaghiosoff and T. Bein, Transformation of amorphous silica colloids to nanosized MEL zeolite, *Microporous Mesoporous Mater.*, 2001, **50**, 121–128.

29 M. Vilaseca, S. Mintova, K. Karaghiosoff, T. H. Metzger and T. Bein, $AlPO_4$-18 synthesized from colloidal precursors and its use for the preparation of thin films, *Appl. Surf. Sci.*, 2004, **226**, 1–6.

30 S. Yang and A. Navrotsky, In situ calorimetric study of the growth of silica TPA-MFI crystals from an initially clear solution, *Chem. Mater.*, 2002, **14**, 2803–2811.

31 N. Pienack and W. Bensch, *In situ* monitoring of the formation of crystalline solids, *Angew. Chem., Int. Ed.*, 2011, **50**, 2014–2034.

32 S. Ueda and M. Koizumi, Crystallization of analcime solid solutions from aqueous solutions, *Am. Mineral.*, 1979, **64**, 172–179.

33 M. K. Choudhary, M. Kumar and J. D. Rimer, Regulating nonclassical pathways of silicalite-1 crystallization through controlled evolution of amorphous precursors, *Angew. Chem., Int. Ed.*, 2019, **58**, 15712–15716.

34 S. Kumar, T. M. Davis, H. Ramanan, R. L. Penn and M. Tsapatsis, Aggregative growth of silicalite-1, *J. Phys. Chem. B*, 2007, **111**, 3398–3403.

35 J. W. Harris, M. J. Cordon, J. R. Di Iorio, J. C. Vega-Vila, F. H. Ribeiro and R. Gounder, Titration and quantification of open and closed Lewis acid sites in Sn-Beta zeolites that catalyze glucose isomerization, *J. Catal.*, 2016, **335**, 141–154.

36 V. Zholobenko, C. Freitas, M. Jendrlin, P. Bazin, A. Travert and F. Thibault-Starzyk, Probing the acid sites of zeolites with pyridine: Quantitative AGIR measurements of the molar absorption coefficients, *J. Catal.*, 2020, **385**, 52–60.

37 T. M. Davis, T. O. Drews, H. Ramanan, C. He, J. Dong, H. Schnablegger, M. A. Katsoulakis, E. Kokkoli, A. V. McCormick, R. L. Penn and M. Tsapatsis, Mechanistic principles of nanoparticle evolution to zeolite crystals, *Nat. Mater.*, 2006, **5**, 400–408.

38 S. Kumar, Z. Wang, R. L. Penn and M. Tsapatsis, A structural resolution Cryo-TEM study of the early stages of MFI growth, *J. Am. Chem. Soc.*, 2008, **130**, 17284–17286.

39 S.-Y. Fang, A. S. T. Chiang and H.-M. Kao, Increasing the productivity of colloidal zeolite Beta by posthydrolysis evaporation, *Ind. Eng. Chem. Res.*, 2010, **49**, 12191–12196.

40 Y. Hu, C. Liu, Y. Zhang, N. Ren and Y. Tang, Microwave-assisted hydrothermal synthesis of nanozeolites with controllable size, *Microporous Mesoporous Mater.*, 2009, **119**, 306–314.

41 L. I. Meza, M. W. Anderson, J. R. Agger, C. S. Cundy, C. B. Chong and R. J. Plaisted, Controlling relative fundamental crystal growth rates in silicalite: AFM observation, *J. Am. Chem. Soc.*, 2007, **129**, 15192–15201.

42 X. Chen, W. Yan, W. Shen, J. Yu, X. Cao and R. Xu, Morphology control of self-stacked silicalite-1 crystals using microwave-assisted solvothermal synthesis, *Microporous Mesoporous Mater.*, 2007, **104**, 296–304.

43 C.-H. Cheng and D. F. Shantz, Silicalite-1 growth from clear solution: Effect of alcohol identity and content on growth kinetics, *J. Phys. Chem. B*, 2005, **109**, 19116–19125.

44 S. Li, J. Li, M. Dong, S. Fan, T. Zhao, J. Wang and W. Fan, Strategies to control zeolite particle morphology, *Chem. Soc. Rev.*, 2019, **48**, 885–907.

45 C. S. Cundy, B. M. Lowe and D. M. Sinclair, Crystallisation of zeolitic molecular sieves: direct measurements of the growth behaviour of single crystals as a function of synthesis conditions, *Faraday Discuss.*, 1993, **95**, 235–252.

46 A. E. Persson, B. J. Schoeman, J. Sterte and J. E. Otterstedt, The synthesis of discrete colloidal particles of TPA-silicalite-1, *Zeolites*, 1994, **14**, 557–567.

47 P. Zhu, J. Wang, F. Xia, W. Zhang, H. Liu and X. Zhang, Alcohol-assisted synthesis of sheet-Like ZSM-5 zeolites with controllable aspect ratios, *Eur. J. Inorg. Chem.*, 2023, **26**, e202200664.

48 S. Bosnar, T. Antonić Jelić, J. Bronić, M. Dutour Sikirić, S. Šegota, V. Čadež, V. Smrečki, A. Palčić and B. Subotić, Deep insights into the processes occurring during early stages of the formation and room-temperature evolution of the core (amorphous SiO_2)@shell (organocations) nanoparticles, *J. Phys. Chem. C*, 2018, **122**, 9441–9454.

49 C.-H. Cheng and D. F. Shantz, ^{29}Si NMR studies of zeolite precursor solutions, *J. Phys. Chem. B*, 2006, **110**, 313–318.

50 S. D. Kinrade, C. T. G. Knight, D. L. Pole and R. T. Syvitski, Silicon-29 NMR studies of tetraalkylammonium silicate solutions. 1. Equilibria, ^{29}Si chemical shifts, and ^{29}Si relaxation, *Inorg. Chem.*, 1998, **37**, 4272–4277.

51 R. Li, A. Smolyakova, G. Maayan and J. D. Rimer, Designed peptoids as tunable modifiers of zeolite crystallization, *Chem. Mater.*, 2017, **29**, 9536–9546.

52 C. Sun, Z. Liu, S. Wang, H. Pang, R. Bai, Q. Wang, W. Chen, A. Zheng, W. Yan and J. Yu, Anionic tuning of zeolite crystallization, *CCS Chem.*, 2021, **3**, 189–198.

53 J. Zhang, R. Bai, Y. Zhou, Z. Chen, P. Zhang, J. Li and J. Yu, Impact of a polymer modifier on directing the non-classical crystallization pathway of TS-1 zeolite: accelerating nucleation and enriching active sites, *Chem. Sci.*, 2022, **13**, 13006–13014.

4058 | *Inorg. Chem. Front.*, 2025, **12**, 4048–4058

This journal is © the Partner Organisations 2025